

Pulsed electron spin resonance spectroscopy in the Purcell regime

V. Ranjan,^{1, a)} S. Probst,¹ B. Albanese,¹ A. Doll,² O. Jacquot,¹ E. Flurin,¹ R. Heeres,¹ D. Vion,¹ D. Esteve,¹ J. J. L. Morton,³ and P. Bertet¹

¹⁾ *Quantronics group, SPEC, CEA, CNRS, Université Paris-Saclay, CEA Saclay 91191 Gif-sur-Yvette Cedex, France*

²⁾ *Laboratoire Nanomagnétisme et Oxydes, SPEC, CEA, CNRS, Université Paris-Saclay, CEA Saclay 91191 Gif-sur-Yvette Cedex, France*

³⁾ *London Centre for Nanotechnology, University College London, London WC1H 0AH, United Kingdom*

(Dated: 20 January 2020)

In EPR, spin relaxation is typically governed by interactions with the lattice or other spins. However, it has recently been shown that given a sufficiently strong spin-resonator coupling and high resonator quality factor, the spontaneous emission of microwave photons from the spins into the resonator can become the main relaxation mechanism, as predicted by Purcell. With increasing attention on the use of microresonators for EPR to achieve high spin-number sensitivity it is important to understand how this novel regime influences measured EPR signals, for example the amplitude and temporal shape of the spin-echo. We study this regime theoretically and experimentally, using donor spins in silicon, under different conditions of spin-linewidth and coupling homogeneity. When the spin-resonator coupling is distributed inhomogeneously, we find that the effective spin-echo relaxation time measured in a saturation recovery sequence strongly depends on the parameters for the detection echo. When the spin linewidth is larger than the resonator bandwidth, the different Fourier components of the spin echo relax with different characteristic times due to the role of the resonator in driving relaxation which results in the temporal shape of the echo becoming dependent on the repetition time of the experiment.

PACS numbers: 07.57.Pt, 76.30.-v, 85.25.-j

I. INTRODUCTION

Pulsed magnetic resonance spectroscopy proceeds by applying sequences of control pulses to an ensemble of electron or nuclear spins via an electromagnetic resonator of frequency ω_0 (at microwave or radio frequency, respectively). Driven by these pulses, the spins undergo nutations on the Bloch sphere. Spins with identical Larmor and Rabi frequencies (forming a *spin packet*) follow the same trajectory. A prominent pulse sequence is the Hahn echo: a first pulse imprints its phase coherence among all spin packets, which quickly vanishes due to the inhomogeneity in Larmor precession frequency. Coherence is restored by a second control pulse applied after a delay τ , which imposes a π phase shift to the spin packets leading to their collective rephasing after another delay τ . This causes the buildup of a macroscopic oscillating magnetization and the emission of a pulse known as the spin-echo, whose amplitude, shape, and time-dependence bear the desired information on spin characteristics and environment¹.

The maximum spin-echo amplitude is governed by the equilibrium spin longitudinal magnetization S_{z0} . After each echo sequence, the spins are strongly out of equilibrium, so that before the next sequence can be started, a waiting time is needed for the longitudinal spin polarization S_z to relax back towards S_{z0} by energy exchange

between each spin and its environment in a characteristic time T_1 .

In solids, the dominant energy exchange processes are usually spin-phonon or spin-spin interactions. For isotropic systems, T_1 depends only on global sample properties (temperature, concentration in magnetic species, ...); as a result, all spin packets contributing to the echo emission relax in the same way². In anisotropic systems, correlations may exist between T_1 and the Larmor frequency of the spins^{1,3}. Spin and spectral diffusion, as well as polarization transfer mechanisms, may also play a role and lead to non-exponential S_z relaxation^{4,5}.

Though much less common in EPR, spins can also, in principle, relax to equilibrium by exchanging energy with the radiation field. In free space, such radiative relaxation is negligibly slow for spins ($\sim 10^{12}$ s at for electron spins at 9 GHz), however, it can however be considerably accelerated by coupling the spin to a resonator. This is known as the Purcell effect, and arises due to the spatial and spectral confinement of the microwave field provided by the resonator⁶⁻⁸. The timescale for spin relaxation resulting from the Purcell effect is a function of the spin-resonator frequency detuning, δ , the resonator energy damping rate κ , and the spin-resonator coupling strength g :

$$T_1 = \frac{\kappa}{4g^2} \left[1 + \left(\frac{2\delta}{\kappa} \right)^2 \right]. \quad (1)$$

Here, g is equal to the half the Rabi frequency for a

^{a)} vishal.ranjan@cea.fr

spin being driven by a resonator field with an average energy of one photon, whose amplitude we denote δB_1 , and $\kappa = \omega_0/Q$ is determined by the resonator frequency and total quality factor. At resonance, $T_1 = \kappa/4g^2$, which shows that Purcell relaxation rate is enhanced for resonators with high quality factor and small mode volume. In usual EPR spectrometers, $g/2\pi \sim 10^{-3}$ Hz, and the Purcell time $\sim 10^8$ s still much longer than typical spin-lattice relaxation times. Recent experiments have demonstrated that it is possible to considerably increase $g/2\pi$ up to $10^2 - 10^3$ Hz by using the modes of superconducting micro-resonators, in which the microwave field is confined at the micron- scale around superconducting electrodes. The main motivation to do so is to enhance the spin detection sensitivity, which scales with g^2 and record sensitivities of $10^2 - 10^3$ spin/ $\sqrt{\text{Hz}}$ have been demonstrated in this way^{9,10}. However, as seen from Eq. 1, radiative relaxation by the Purcell effect becomes unavoidably enhanced in these regimes up to the point where it may become the dominant relaxation channel for spins that have long enough spin-lattice relaxation times. This Purcell regime was reached recently for an ensemble of electron spins coupled to a superconducting micro-resonator at millikelvin temperatures^{11,12}. It was furthermore shown to enable electron spin hyperpolarization by radiative cooling¹³.

Given the increasing use of micro-resonators in EPR which are capable of achieving substantial spin-resonator coupling, it is important to understand any significant influences which the Purcell relaxation regime may impose on typical pulsed EPR measurements. For example, one noticeable aspect of Eq. 1 is that Purcell relaxation is a resonant phenomenon, with a strong frequency dependence over a scale given by the resonator linewidth κ ^{11,12}. Another consequence of Eq. 1 is that T_1 depends on the position r of a given spin within the resonator mode, since g is proportional to the field mode amplitude $\delta B_1(r)$. Therefore, in the Purcell regime, spin packets with different detuning and Rabi frequency also have a different relaxation time T_1 , an unusual situation in magnetic resonance. Because a spin echo is the sum of the contribution of all spin packets, spin-echo relaxation is expected to display a complex behavior, particularly when either the Larmor frequency or the Rabi frequency is inhomogeneously distributed, which happens with superconducting micro-resonators whose B_1 field is often spatially-inhomogeneous.

It is the purpose of this article to analyze the implications of these correlations between relaxation time, detuning and Rabi frequencies on the shape and time-dependence of the spin-echo in the Purcell regime. We first provide a simplified model that yields analytical results for the spin-echo amplitude and shape in the Purcell regime, and enables us to identify qualitatively novel effects. When the Rabi frequency is inhomogeneously distributed, the spin-echo amplitude is found to come back to equilibrium with an approximately exponential temporal dependence, but with a time constant that depends

on the control pulse amplitude. When the Larmor frequency is inhomogeneously distributed over a frequency range broader than the resonator linewidth, the various Fourier components of a spin echo relax with different time constants, which also implies that the echo shape becomes dependent on the waiting time between consecutive sequences. The third section describes the experimental setup and samples used to test these effects, and the fourth section presents the measurements, their qualitative agreement with our simplified model, and their quantitative agreement with the simulation of the Bloch equations including explicitly the Purcell decay contribution.

II. SPIN-ECHO IN THE PURCELL REGIME : A SIMPLE MODEL

In this section we analyze a simple model which exemplifies the consequences of Purcell relaxation by considering analytically-tractable limiting scenarios.

A. System description and equations of motion

The system to be modelled is shown in Fig. 1. An ensemble of spins $S = 1/2$ interact with the microwave field inside the resonator used for inductive detection, which is capacitively coupled to a measurement line. The resonator is characterized by its frequency ω_0 , and total energy damping rate κ . Energy is lost by leakage into the measurement line (with a rate $\kappa_c = \omega_0/Q_c$) and internal losses (rate $\kappa_i = \omega_0/Q_i$), with $\kappa = \kappa_c + \kappa_i$. Control pulses at ω_0 are sent to the resonator input through the measurement line, into which the subsequent spin echo signals are emitted then routed via a circulator towards the detection chain.

Each of the $j = 1, \dots, N$ spins is characterized by its Larmor frequency ω_j (or equivalently the spin-cavity detuning $\delta_j = \omega_j - \omega_0$) and its coupling to the resonator field g_j . In the weak spin-resonator coupling limit $g_j \ll \kappa$, the spin-resonator quantum correlations can be neglected. The dynamics is well described by equations involving only the expectation value of the spin and resonator field operators¹⁴, written in the frame rotating at ω_0 as

$$\begin{cases} \dot{S}_x^{(j)} = -\delta_j S_y^{(j)} + 2g_j Y S_z^{(j)} - S_x^{(j)}/T_2^{(j)} \\ \dot{S}_y^{(j)} = \delta_j S_x^{(j)} - 2g_j X S_z^{(j)} - S_y^{(j)}/T_2^{(j)} \\ \dot{S}_z^{(j)} = 2g_j X S_y^{(j)} - 2g_j Y S_x^{(j)} - (S_z^{(j)} - S_{z0})/T_1^{(j)}. \end{cases} \quad (2)$$

Here, $S_{x,y,z}^{(j)}$ is the expectation value of the corresponding dimensionless spin j operator (with $S_{x,y,z}^{(j)} = \sigma_{x,y,z}/2$, $\sigma_{x,y,z}$ being the Pauli operators) and X, Y is the expectation value of the intra-resonator field operators expressed in dimensionless units¹⁴. Here we use the convention that $X = (a + a^\dagger)/2$ and $Y = i(a - a^\dagger)/2$, a (resp. a^\dagger) being the resonator annihilation (resp. creation) operator,

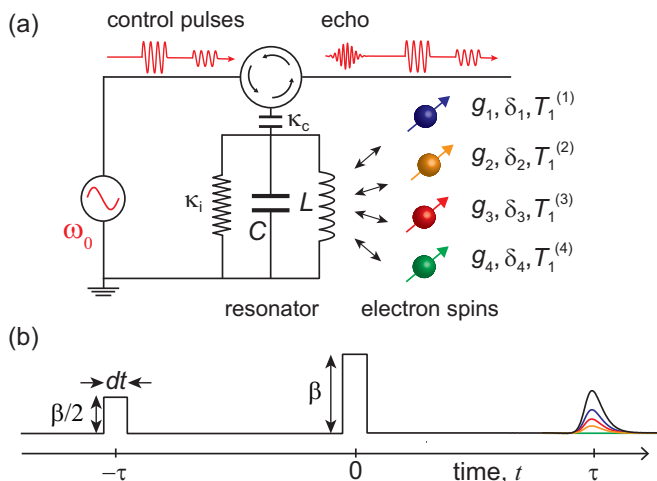


FIG. 1. A Sketch of electron-spin resonance spectroscopy in the Purcell regime. (a) An ensemble of spins is detected via a resonator of frequency ω_0 . Each spin can have a different coupling strength g_j and frequency detuning δ_j with the resonator, which leads to different individual Purcell relaxation time constants $T_1^{(j)}$. The resonator has an internal energy decay rate κ_i and is coupled to a drive and measurement line with an energy decay rate κ_c . (b) A typical Hahn echo sequence with rectangular pulses. Final echo contains contributions from different spin packets. The relative amplitude of contributions depends on experimental parameters such as the pulse amplitude β and the repetition rate.

which differs from the one used in Refs. 14 and 15 by a factor 2. Phase coherence of spin j relaxes in a time $T_2^{(j)}$, and $S_z^{(j)}$ relaxes towards the thermal equilibrium polarization $S_{z0} = \tanh(\hbar\omega_0/2kT_s)$ in a time $T_1^{(j)}$. Because we are specifically interested in the impact of Purcell relaxation on spin-echo signals, we will in the following consider that the only decoherence mechanism is the Purcell relaxation, implying that $T_1^{(j)} = \frac{\kappa}{4g_j^2} [1 + (\frac{2\delta_j}{\kappa})^2]$ and $T_2^{(j)} = 2T_1^{(j)}$.

Note that these equations are identical to the usual Bloch equations, with the Rabi frequency given by $2g_j\alpha(t)$, and $\alpha(t) \equiv \sqrt{X(t)^2 + Y(t)^2}$. Purcell relaxation appears as a T_1 mechanism, and its particular features arise from the dependence of T_1 on the properties of a spin packet.

Using standard input-output theory¹⁶, the resonator field in the rotating frame at ω_0 obey Eqs.

$$\begin{cases} \dot{X}(t) = \sqrt{\kappa_c}\beta_X(t) - \frac{\kappa}{2}X(t) - \sum_{j=1}^N g_j S_y^{(j)} \\ \dot{Y}(t) = \sqrt{\kappa_c}\beta_Y(t) - \frac{\kappa}{2}Y(t) + \sum_{j=1}^N g_j S_x^{(j)}, \end{cases} \quad (3)$$

where $\beta_{X,Y}(t)$ are the in-phase and out of phase components of the control field. We also need to compute the field leaking out of the cavity, as it contains the spin free-induction-decay and echo signals. The output field components $X_{\text{out}}(t), Y_{\text{out}}(t)$ are given by the input-output relations

$$\begin{cases} X_{\text{out}}(t) = \sqrt{\kappa_c}X(t) - \beta_X(t) \\ Y_{\text{out}}(t) = \sqrt{\kappa_c}Y(t) - \beta_Y(t). \end{cases} \quad (4)$$

The combination of Eqs. 1 to 4 is the theoretical framework that describes EPR spectroscopy in the Purcell regime. All the specific characteristics of the spin ensemble are provided by the distributions of Larmor frequency $\rho_\delta(\delta)$ and coupling constant $\rho_g(g)$, normalized such that $\int dg\rho_g(g) = \int d\delta\rho_\delta(\delta) = 1$. We also define Γ as the standard deviation of ρ_δ , thus corresponding to the spin ensemble inhomogeneous linewidth.

Although this is not immediately apparent, we note that radiation damping is automatically included in the above equations, since they treat on an equal footing the intra-resonator field and the spin operators and thus incorporate all feedback effects of the radiation field on the spin dynamics^{14,17}. This underlines the distinction between radiative damping and Purcell relaxation, which both are radiative effects but with different characteristics and impact on the spin dynamics.

Throughout this article, we make the extra simplifying hypothesis that the spin-ensemble cooperativity $C = \sum g_j^2/(\kappa\Gamma)$ verifies $C \ll 1$. In this limit, the field generated by the spins is small compared to the intra-resonator field¹⁸ so that radiation damping can be entirely neglected. One can thus 1) compute the intra-resonator field $[X(t), Y(t)]$ using Eq. 3 with the last term neglected, 2) use it to solve the spin dynamics (Eq. 2), and 3) compute the output field with Eqs. 3 and 4. This is the approach that is used to simulate numerically the spin-echo signals under arbitrary control pulse sequences, and in the next sections to derive approximate expressions for the echo amplitude. More details on the simulations can be found in the Appendix.

B. Hahn echo amplitude

We now derive an approximate analytical expression for the amplitude of a Hahn echo, based on Eqs. 1 to 4 and a number of simplifying assumptions.

To simplify the discussion, we suppose that the control pulses generate a quasi-instantaneous intra-resonator field with a simple rectangular time-dependence of duration dt . This can be achieved if $dt \gg \kappa^{-1}$, or by using shaped pulses that compensate for the finite resonator response time^{14,15,19}. We thus consider input pulses on the in-phase X direction, with an amplitude $\beta_X \equiv \beta$ during dt while $\beta_Y = 0$, related to the input power P_{in} as $\beta = \sqrt{P_{\text{in}}/\hbar\omega_0}$. The corresponding intra-resonator field amplitude is $\alpha = 2\sqrt{\kappa_c}\beta/\kappa$.

Under each control pulse, spin j undergoes a Rabi nutation¹ with a frequency $\sqrt{(2g_j\alpha)^2 + \delta_j^2}$. We assume that $\Gamma \ll 2g_j\alpha$ for all spins so that the dependence of the Rabi frequency on δ_j can be neglected. Also, we assume that ρ_δ is symmetric and is excited in its centre.

The Hahn-echo pulse sequence is shown in Fig. 1. A first pulse of amplitude $\beta/2$ and duration dt is followed by a waiting time τ , then by a second pulse of amplitude β and same duration, and by a second waiting time t . An echo is formed around $t = \tau$ because of the refocusing of the spin packets (we assume $dt \ll \tau$). We also use an equivalent Hahn-echo sequence where the two pulses have the same amplitude β , but the first pulse duration is $dt/2$. The spin-echo originates solely from the y component of the magnetization, and the contribution of spin j can be shown^{1,20} to be

$$S_y^{(j)}(\tau + t) = -S_z^{(j)} \sin^3(2\alpha g_j dt) \cos \delta_j(t - \tau). \quad (5)$$

where $S_z^{(j)}$ is spin j longitudinal polarization at the time of the first control pulse. The latter is not necessarily equal to S_{z0} because the waiting time since the previous pulse sequence may not be sufficiently long. Importantly, because of Purcell relaxation, $S_z^{(j)}$ depends on g_j and δ_j , which leads to novel effects as shown below. Note that we have, however, neglected the impact of spin relaxation during the Hahn echo sequence, because in most relevant scenarios $\tau \ll T_1^{(j)}$.

To obtain simple expressions for the echo amplitude, we also consider that the resonator field dynamics adjusts adiabatically to the spin operators, as would be the situation in the limit of low resonator Q . Equations 3 and 4 then yield

$$\begin{aligned} X_{\text{out}}(\tau + t) &= -2 \frac{\sqrt{\kappa_c}}{\kappa} \sum_j g_j S_y^{(j)}(\tau + t) \\ &= -2 \frac{\sqrt{\kappa_c}}{\kappa} \int \int g \rho_g(g) \rho_\delta(\delta) S_y(g, \delta, t) d\delta dg, \quad (6) \end{aligned}$$

where we have taken the continuous limit in the last expression and defined $S_y(g, \delta, t)$ as being equal to $S_y^{(j)}(\tau + t)$ for a spin j having a coupling $g_j = g$ and detuning $\delta_j = \delta$. Note also that we have implicitly assumed that there is no correlation between the frequency of a given spin and its coupling constant g , an assumption that is not always verified²¹.

This echo amplitude $X_{\text{out}}(t + \tau)$ depends in an intricate way on the pulse amplitude and on the shape of the inhomogeneous distributions ρ_g and ρ_δ . In the following we consider two limiting cases.

C. Narrow-line case

Let us first assume that the spin ensemble has a linewidth much narrower than the resonator, ie $\Gamma \ll \kappa$. Then, $T_1 \approx \kappa/(4g^2)$, implying that S_z and S_y do not depend any longer on δ . Overall, the echo amplitude at $t = \tau$ becomes

$$X_{\text{out}}(2\tau) = 2 \frac{\sqrt{\kappa_c}}{\kappa} \int g S_z \rho_g(g) \sin^3(2\alpha g dt) dg. \quad (7)$$

To appreciate the impact of Purcell relaxation, we now focus on the so-called saturation recovery sequence schematically depicted in Fig. 2c, which is commonly used to measure spin relaxation time. It consists of applying a saturating pulse at time $t = 0$ (so that $S_z(t = 0) = 0$ for all spins), followed by a Hahn-echo sequence applied after a waiting time T at $t = T$. Its maximum amplitude at time $t = T + 2\tau$ is denoted by $X_{\text{out}}(T)$ for simplicity in the following. At the beginning of the Hahn-echo sequence,

$$S_z(T) = S_{z0} \left(1 - e^{-T/T_1}\right). \quad (8)$$

In the usual situation where spin relaxation is not Purcell-limited or when it is governed by interactions with the lattice, and where the system is moreover isotropic, all spins then relax with the same time constant T_1 . In Eq. 7, S_z can be factorized; the echo amplitude is proportional to $S_z(T)$, and it follows the exponential dependence of $S_z(T)$, which enables to measure T_1 . The echo amplitude effectively measures the longitudinal polarization $S_z(T)$, which justifies its denomination as a *detection echo*; in particular, its parameters (pulse amplitude, duration, ...) have no impact on the measured T_1 .

In the Purcell regime, T_1 is different for spin-packets with different couplings g ; the detection echo amplitude $X_{\text{out}}(T)$ has thus no reason to be even exponential. Because of the strong g -dependence of the integrand in Eq. 7 however, an approximate exponential dependence is nevertheless recovered in a number of situations, but with an effective relaxation time that now depends on the parameters of the detection echo.

We now make this reasoning explicit by considering three types of coupling constant distributions ρ_g shown in Fig. 2. The spins may be located in an area where B_1 is very homogeneous (type A), or on the contrary very inhomogeneous (types B and C). To consider situations encountered in recent experiments, we assume that B_1 is generated by a narrow wire deposited at the surface of a sample containing the spins. The spins may be distributed within a thin layer just below the sample surface (type B), or homogeneously in the bulk (type C). Assuming that $\delta B_1(r) = \mu_0 \delta i / (2\pi r)$, r being the spin-wire distance and δi the quantum fluctuations of the ac current in the resonator, it is straightforward to see that $\rho_g(g) = \delta(g - g_A)$ in type A, $\rho(g) = g_B/g^2$ in type B, and $\rho(g) = g_C^2/g^3$ in type C.

For completeness, it is interesting to note that the situation may be complicated by the presence of correlations between the spin Larmor and Rabi frequency. This was reported in Ref. 9 and 11. There, silicon donor spins were confined to a thin layer (100 nm) below the surface

of a silicon sample, on top of which a thin-film resonator with a $5\mu\text{m}$ -wide inductance was deposited. Because of the mechanical strain exerted by the thin metallic film on the silicon substrate²¹ due to differential thermal contractions between the metal and the silicon, the spin hyperfine interaction becomes correlated with the lateral position relative to the wire, which also happens to be approximately correlated to B_1 . As a result, the Larmor and Rabi frequencies of the spins are correlated, and by properly choosing the biasing field B_0 the system is much better described by type A than type B. This approximate correlation is valid only when the wire transverse dimensions are large compared to the spin layer thickness, and was indeed no longer found in Ref. 10 where the wire width was decreased to 500 nm.

We will now compute the signal expected from a saturation recovery sequence for three afore-mentioned types of spin distribution, by inserting Eq. 8 into Eq. 7.

In type A, we obtain straightforwardly

$$X_{\text{out}}(T) = 2 \frac{\sqrt{\kappa_c}}{\kappa} g_A \sin^3(2\alpha g_A dt) S_{z0} (1 - \exp^{-\frac{T}{T_1(g_A)}}). \quad (9)$$

Because the coupling constant has a well-defined value g_A , the spin relaxation time is identical for all measured spins and we are in the same situation as in usual magnetic resonance, where the detection echo amplitude relaxes exponentially with the Purcell relaxation time $T_1(g_A)$, independently of α .

To deal with types B and C, it is useful to introduce the Rabi nutation angle $\psi = 2\alpha g dt$. The T dependent echo amplitude can then be written as

$$X_{\text{out}}(T) = 2 \frac{\sqrt{\kappa_c}}{\kappa} S_{z0} \int [1 - \exp^{-\frac{T}{T_1(\alpha, \psi)}}] f(\psi) d\psi, \quad (10)$$

with $T_1(\alpha, \psi) = \frac{\kappa \alpha^2 dt^2}{\psi^2}$ and $f(\psi) = \psi \rho_\psi \sin^3 \psi / (2\alpha dt)$. The function $f(\psi)$ indicates the relative contribution of spin packets to the total echo signal as a function of their Rabi angle ψ . As shown in Fig. 2 for types B and C, it displays a maximum at a value ψ_0 close to $\pi/2$. In a crude approximation, $f(\psi) \sim \delta(\psi - \psi_0)$, so that

$$X_{\text{out}}(T) = 2 \frac{\sqrt{\kappa_c}}{\kappa} S_{z0} (1 - \exp^{-\frac{T}{T_1(\alpha, \psi_0)}}). \quad (11)$$

Despite the broad coupling constant distribution, one thus recovers an approximate exponential dependence of the detection echo amplitude on the waiting time T . However, the effective measured relaxation time scales like α^2 , the square of the amplitude of the pulse used in the detection echo sequence. The physical interpretation is straightforward: the detection echo signal mostly originates from the contribution of spins that undergo first a $\pi/2$ pulse and then a π pulse during the refocusing step. When the pulse amplitude is varied, this amounts

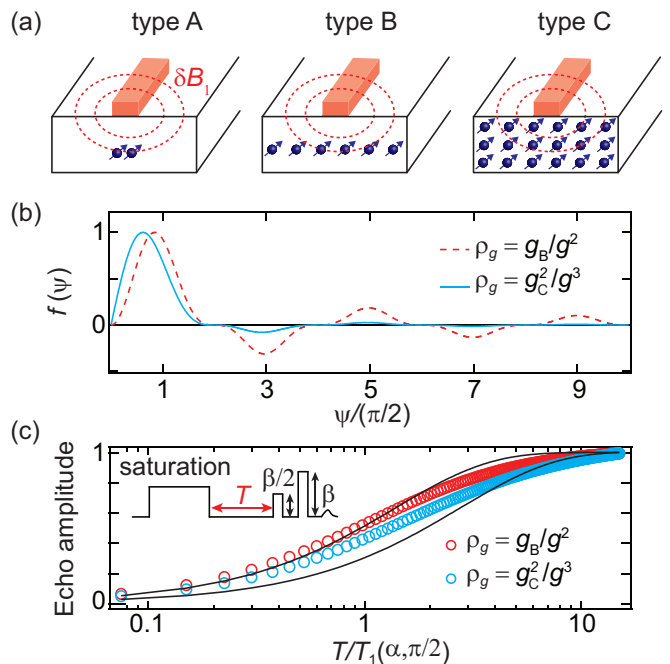


FIG. 2. Rabi angle selectivity in the narrow line case. (a) Types of spin implantation in the substrate, type A: point distribution, type B: thin layer distribution, type C: bulk distribution. Contours of rf magnetic field B_1 created by the inductor are sketched as dashed curves. (b) Calculated relative echo contribution $f(\psi)$ from spin packets with different Rabi angle ψ . (c) Saturation recovery of the echo amplitude calculated using the model. We have taken small Rabi angles $0 < \psi < \pi$. Solid black curves show exponential recovery of polarization with a decay constant $T_1(\alpha, \psi_0)$, where ψ_0 is the value where $f(\psi)$ is maximum in panel (b).

to selecting spins with different coupling constants g , and therefore different relaxation times.

To verify the validity of approximating $f(\psi)$ by a δ function, we compute Eq. 10 numerically for types B and C. The results are shown in Fig. 2(c) for the decay of the spin-echo amplitude $A(T)$ (open circles), compared to the single-exponential approximation of Eq. 11 (solid lines, taking into account the different values of ψ_0 for types B and C). The qualitative agreement demonstrates that Eq. 11 correctly captures the impact of Purcell relaxation on the effective relaxation time measured in a saturation-recovery sequence.

D. Narrow-coupling case

We now consider the case where the coupling constant is single-valued (corresponding to type A in the previous section) $\rho_g(g) = \delta(g - g_A)$. The pulse amplitude is chosen such that $2g_A \alpha dt = \pi/2$, so that the control pulses implement the ideal Hahn-echo sequence. The Larmor frequency on the other hand is broadly distributed, with $\Gamma \gg \kappa$.

In that limit, the Hahn echo amplitude Eq. 6 becomes

$$X_{\text{out}}(\tau + t) = 2 \frac{\sqrt{\kappa_c}}{\kappa} \int S_z \rho_\delta \cos \delta(t - \tau) d\delta. \quad (12)$$

Consider now that the echo sequences are repeated multiple times, with a waiting time T in-between two consecutive sequences, and let us assume that the spins are fully un-polarized at the immediate end of a sequence, $S_z = 0$. Then at the beginning of each echo, the longitudinal polarization S_z is given by Eq. 8.

In a usual situation where T_1 is not correlated with the spin Larmor frequency, S_z can be factored out of the integral in Eq. 12, and the echo temporal shape is simply given by the Fourier transform of the Larmor frequency distribution $\rho_\delta(\delta)$.

In the Purcell regime however, we get that

$$S_z = S_{z0} (1 - e^{-T/T_1(\delta)}), \quad (13)$$

so that

$$X_{\text{out}}(\tau + t) = 2 \frac{\sqrt{\kappa_c}}{\kappa} S_{z0} \times \int (1 - e^{-T/T_1(\delta)}) \rho_\delta(\delta) \cos \delta(t - \tau) d\delta, \quad (14)$$

whose Fourier transform is

$$\tilde{X}_{\text{out}}(\delta, T) = 2 \frac{\sqrt{\kappa_c}}{\kappa} S_{z0} (1 - e^{-T/T_1(\delta)}) \rho_\delta(\delta). \quad (15)$$

The Fourier components $\tilde{X}_{\text{out}}(\delta)$ of the echo therefore relax with a time constant $T_1(\delta)$ that follows the Purcell effect, and should thus increase with detuning quadratically.

Moreover, the spin-echo temporal shape is given by the Fourier transform of $\rho_\delta(\delta) (1 - e^{-T/T_1(\delta)})$, which now depends on the repetition time T . The interpretation is here again straightforward. Because of the dependence of the relaxation time on the detuning, the physical spin distribution $\rho_\delta(\delta)$ is effectively renormalized by the factor $(1 - e^{-T/T_1(\delta)})$. At short times $4g_A^2 T \ll \kappa$, $(1 - e^{-T/T_1(\delta)}) \simeq T/T_1 = 4g^2 T / \kappa \times 1/(1 + 4\delta^2/\kappa^2)$, implying that the effective spin distribution is given by the resonator filter function. In the long time limit $4g_A^2 T \gg \kappa$, this effective distribution is closer to the physical spin distribution function $\rho_\delta(\delta)$. Note that this Purcell-filtering of the spin distribution should not be mistaken for the electromagnetic filtering of the spin-echo signal by the cavity, which will always be there in a real experiment but was neglected here for simplicity because of the low-Q assumption.

III. MATERIALS AND METHODS

We now describe the sample and setup used to demonstrate the effects discussed above. Reaching the Purcell regime requires spins with long intrinsic spin relaxation times, and resonators with a small mode volume and high quality factor. Bismuth donors in silicon at millikelvin temperature have an intrinsic relaxation time $T_{1,\text{int}} = 1500$ s, and are thus in the Purcell regime whenever $T_1 \ll T_{1,\text{int}}$. This was shown in Ref. 11, where $T_1 = 1$ s was reached when the bismuth donors were at resonance with a high-quality-factor superconducting micro-resonator. All the measurements reported in this article are also in this Purcell regime.

We present data from three different devices. Each device is a silicon sample that was implanted with bismuth atoms close to its surface, and on which a discrete-element superconducting LC resonator was patterned. The resonators consist of an interdigitated capacitance shunted by a micron- or sub-micron-scale wire which plays the role of the inductance [Fig. 3(a-c)]. The devices are mounted in a copper sample holder, and coupled capacitively to a microwave antenna which determines the coupling rate κ_c . In devices 1 and 2 [Fig. 3(d-e)], the implantation depth is ~ 100 nm, with a peak concentration of $8 \times 10^{16} \text{ cm}^{-3}$, the silicon sample is isotopically enriched in ^{28}Si , and the resonator is made in aluminum. In device 3 [Fig. 3(f)], the implantation depth is $\sim 1 \mu\text{m}$, with a smaller peak concentration of 10^{16} cm^{-3} , the silicon is of natural isotopic abundance, and the resonator is made of niobium. Of particular importance for this work is the geometry of the resonator inductance, which strongly impacts the coupling constant distribution $\rho_g(g)$. It is 100 nm wide and 10 μm long in device 1, 500 nm wide and 100 μm long in device 2, and 2 μm wide and 700 μm long in device 3. The characteristics of the devices are summarized in Table I.

Bismuth atoms implanted in the silicon form four covalent bonds to the silicon lattice, while the fifth valence electron is trapped at low temperatures by the hydrogenic potential formed by the ionized bismuth atom; its spin gives rise to the ESR signal²². Due to the hyperfine interaction between the unpaired electron spin and the bismuth nuclear spin, allowed ESR transitions are found close to ~ 7.38 GHz at small magnetic fields. More details on the spin Hamiltonian and ESR transitions can be found in the Appendix B. In our devices, bismuth donor spins experience large strain when cooled to low temperature because of the differential thermal expansion of Al and Si^{21,23}, which leads to ESR lines much broader than both κ and the Rabi frequency $2g\alpha$ in our experiments. We model this by a constant distribution ρ_δ .

The coupling constant distribution $\rho_g(g)$ is computed by first estimating the rms current fluctuations in the inductance $\delta i_0 = \omega_0 \sqrt{\hbar/2Z_0}$, where the LC resonator impedance $Z_0 = \sqrt{L/C}$ is extracted from electromagnetic simulations. This yields the position dependence of the rms magnetic field fluctuations $\delta B_1(r)$ and of the cou-

TABLE I. Device parameters

	Device 1	Device 2	Device 3
Substrate	^{28}Si	^{28}Si	natural Si
^{29}Si in substrate (%)	0.05	0.05	4.7
N_{max} (cm^{-3})	8×10^{16}	8×10^{16}	10^{16}
Implantation depth (μm)	~ 0.1	~ 0.1	~ 1
Resonator material	Al	Al	Nb
Inductor width (μm)	0.1	0.5	2
Inductor length (μm)	10	100	700
$\omega_0/2\pi$ (GHz)	7.25	7.25	7.41
Q_i	8×10^4	2×10^5	2×10^5
Q_c	3×10^4	7×10^4	10^4
$Q = Q_i Q_c / (Q_i + Q_c)$	2×10^4	5×10^4	10^4
Z_0 (Ω)	15	30	40
B_0 (mT)	3.7	3.7	62.5
π pulse duration (μs)	1	1	0.25
Peak pulse power (pW)	0.1	1	1000

pling constant $g(r) = \gamma_e \langle 0 | S_x | 1 \rangle | \delta B_1(r) |^{24}$ [see Fig. 3(d-f)]. Combined with the implantation profile, we then estimate the coupling constant distribution $\rho_g(g)$ for all three devices [solid lines in Fig. 3(g)]. At small g , $\rho_g(g)$ scales like g^{-2} in all devices, as expected from the analysis of section IIC for type *B*. This dependence breaks down for spins that are close to the wire (and have therefore the largest coupling to the resonator), and become sensitive to its transverse dimension, which leads to a cut-off in $\rho_g(g)$. This cutoff lies at about 4 kHz, 0.8 kHz, and 0.1 kHz for devices 1 to 3. Because the inductor wire is larger than the spin implantation depth in devices 2 and 3, ρ_g features a shoulder at about 0.6 kHz and 0.06 kHz respectively, due to the significant density of spins lying right below the wire and therefore seeing a more uniform B_1 field; in a sense, these devices are intermediate between types *A* and *B*.

The samples are cooled to 20 mK in a dilution refrigerator, and measured in a setup described schematically in Fig. 4. Control pulses are sent at ω_0 through an input line that incorporates low-temperature attenuation, and the reflected pulses together with the spin echo signal are routed by a circulator towards a parametric amplifier at 10 mK (either of the JPA²⁵ or the JTWPA²⁶ type). After further amplification at 4 K by a High-Electron-Mobility Transistor amplifier and at 300 K, the output signal is homodyne demodulated by mixing with a local oscillator also at ω_0 , yielding the echo signal $X_{\text{out}}(t + \tau)$ used for analysis. Details of pulse frequency, duration and power are summarized in table I. We remark that transient heating from pulses is negligible in our setup.

All three resonators have slightly different frequencies ω_0 , all within 200 MHz of 7.37 GHz, the zero-field splitting of bismuth donors in silicon. The resonators are

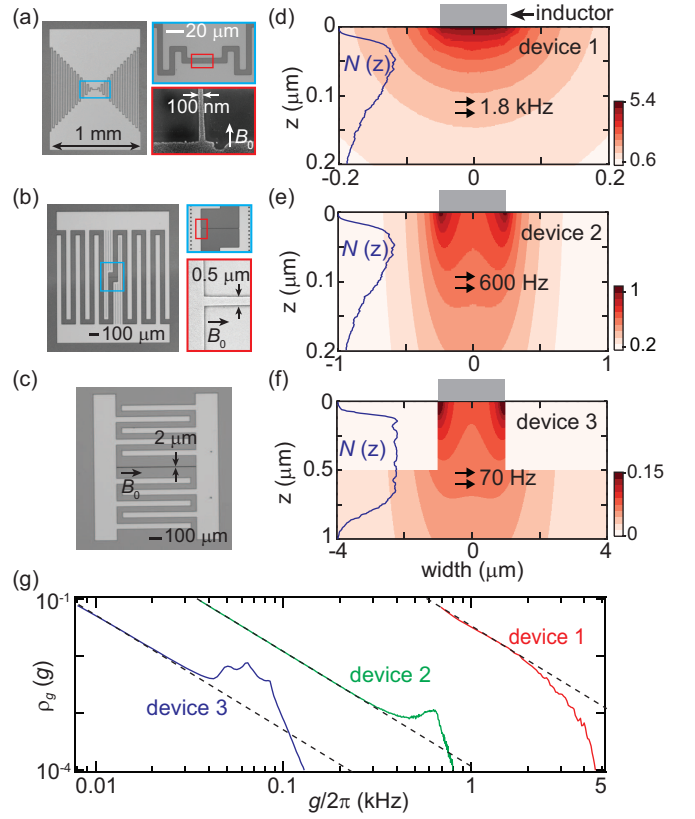


FIG. 3. Device details. (a-c) Optical photographs of the three LC resonators, and scanning electron microscopy images of the sub- μm wide inductors for devices 1 and 2. The direction of the static magnetic field B_0 is also shown. (d-f) Calculated coupling strength $g/2\pi$ (in kHz) distribution (color contour plots) for the 3 devices. The Bi dopants are implanted homogeneously over the whole sample area with an implantation profile $N(z)$ (left trace); the spin signal originates dominantly from spins located directly below the inductor. In panel (f), white rectangular areas on two sides of the inductor represent regions that have been etched during fabrication. (g) Log-log plot of calculated coupling distribution $\rho_g(g)$. Dashed lines represent $1/g^2$ dependence.

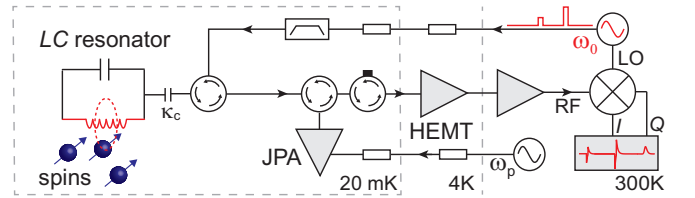


FIG. 4. Schematic of the measurement setup at different temperature stages of our ESR spectrometer.

in the overcoupled regime ($\kappa_c \gg \kappa_i$), with total quality factors in the $10^4 - 10^5$ range. A magnetic field B_0 is applied parallel to the sample, along the inductor wire, and its value is chosen such that one of the bismuth donor transitions is resonant with ω_0 .

IV. EXPERIMENTAL RESULTS

A. Pulse-amplitude-dependent spin relaxation

We use device 1 to investigate the dependence of T_1 on the excitation amplitude β predicted in section 2C when ρ_g is broadly distributed. As discussed earlier, in device 1 ρ_g corresponds well to type *B* so that the analysis of Section IIC should apply.

Saturation recovery pulse sequences are applied, with a saturation pulse of duration 2 ms and fixed amplitude, followed after a variable delay T by a detection echo. Square input pulses of duration 1 μs are used, of respective amplitudes $\beta/2$ and β . To more closely approximate the narrow-line hypothesis of Section 2C, the echo signal $X_{\text{out}}(t + \tau)$ is integrated over its duration T_E yielding the echo area $A_e(T) = \int_{-T_E/2}^{+T_E/2} X_{\text{out}}(t + \tau) dt$, which is equal to the zero-detuning Fourier component and thus contains the contribution of spins at resonance with the resonator.

The resulting $A_e(T)$ is shown in Fig. 5(a), for two different values of β . We see that both datasets are satisfactorily fitted by exponentially decaying curves, but with different time constants T_1 . Figure 5(b) shows the measured $T_1(\beta)$, which scales like β^2 as predicted in section IIC. We also measured T_1 using an inversion recovery sequence [see Fig. 5(c)], using an inversion pulse with the same amplitude and duration as the refocusing pulse of the detection echo. Here for each data point, we wait 30 ms between the echo detection and start of the next sequence. The fitted T_1 values are identical to the saturation-recovery ones within error bars and display the same β^2 scaling. Note that this would probably not hold if the inversion pulse amplitude was too different from β .

In order to compare the experiments to simulations, an absolute calibration of the input pulse amplitude β is needed. Since attenuation and filtering along the input line cannot be known precisely enough, the calibration is performed by comparing the Rabi simulations to the dedicated Rabi pulse sequence shown in Fig. 6. A first pulse of varying amplitude drives Rabi oscillations in the spin ensemble followed, after a waiting time of 1 ms, by detection echo. The frequency and amplitude of the resulting oscillations are compared to the simulation, which calibrates β (see Fig. 6). Using this independent calibration, we simulate the saturation recovery experiment of Fig. 5, taking into account the estimated ρ_g and ρ_δ for device A. Both the shape of the relaxation curves $A_e(T)$ and the dependence of the fitted T_1 on β are well reproduced, without adjustable parameters.

To confirm the interpretation given in Section IIC, we show in Fig. 5(d) the relative contribution to the echo of various spin packets as a function of the value of their coupling constant g , extracted from the simulations for the two example curves shown in Fig. 5 at a waiting time $T = 30$ ms larger than T_1 , so that the spins are close to

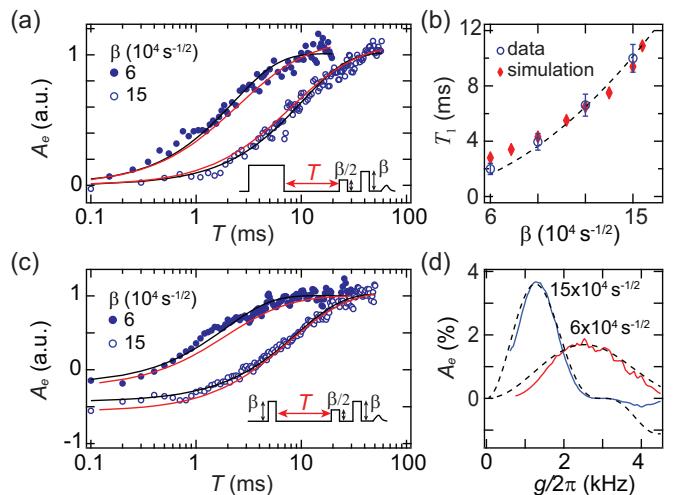


FIG. 5. Spin relaxation versus excitation amplitude (device 1). (a) Relaxation of the echo area $A_e(T)$ as a function of the waiting time T in a saturation recovery sequence (shown in inset), for two different values of β . Circles and red lines correspond to measurements and numerical simulations. Black lines correspond to least square fits of the data by single-exponentials. (b) Comparison of experimentally extracted T_1 values (open blue circles) with simulated ones (red diamonds), for more β values. The dashed line is a quadratic fit to the data. (c) Spin relaxation measurements using inversion recovery method. (d) Calculated contribution (solid lines) of spin packets with coupling g to the echo amplitude $A_e(T = 30\text{ms})$, for the saturation recovery sequence and the two β values of a). Dashed lines represent the corresponding $f(\psi)$ function introduced in the model section.

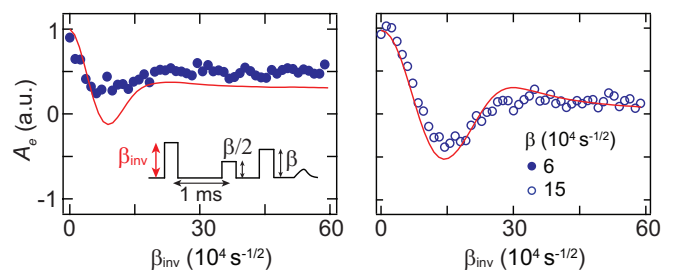


FIG. 6. Rabi oscillations measured (circles) for two different values of pulse amplitude β (see sequence in inset), using device 1. The fit to the data of simulations (solid red lines) provides a calibration of β .

equilibrium. As expected, an echo obtained with a larger pulse amplitude (large β) has more contributions from spins that are more weakly coupled, compared for the echo using weaker pulses (smaller β). On the same figure we also show $f(\psi)$, and observe a satisfactory agreement with our simple model.

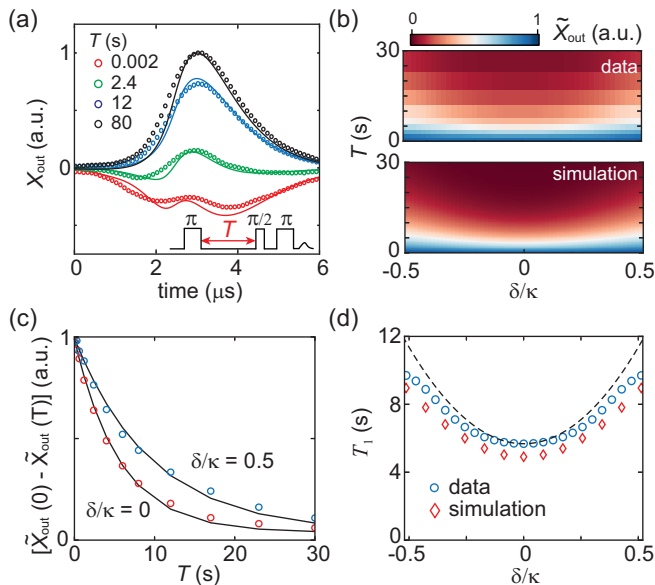


FIG. 7. Spin relaxation versus detuning (device 3). (a) Echoes measured at different delays T of an inversion recovery sequence (inset) applied to device 3. Simulations shown as solid lines take into account the corresponding $\rho_g(g)$ (see Fig. 3g). (b) Color maps of measured and simulated spin relaxation $\tilde{X}_\delta(T)$ at different spin detunings δ . (c) Exponential fits (lines) and the data (circles) for two values of δ/κ . (d) Comparison of measured $T_1(\delta)$ (open blue circles) with simulation without adjustable parameters (open red diamonds). The dashed line shows the expected $T_1(\delta)$ dependence based on the Purcell formula Eq. 1 and on the measured T_1 at $\delta = 0$.

B. Detuning dependent spin relaxation

We investigate the detuning dependence of spin relaxation with devices 2 and 3 in which the coupling constant distribution shows a plateau (Fig. 3), so that they approach the narrow-coupling limit described in Section IID and display well-defined Rabi oscillations allowing us to perform Rabi nutations with a well-defined angle¹⁰.

The inversion recovery sequence is first applied to device 3 (see Fig. 7). The echo signal $X_e(t + \tau)$ is shown in Fig. 7(a) for various values of the waiting time T . As expected, its phase is inverted for short values of T compared to long ones.

The Fourier transform of each curve $\tilde{X}_e(\delta)$ is then computed as shown by colormaps in Fig. 7(b). Figure 7(c) shows the time dependence of two normalized Fourier components ($\delta = 0$ and $\delta = 0.5\kappa$) and demonstrates that $\tilde{X}_{\delta=0}(T)$ relaxes faster than $\tilde{X}_{\delta=0.5\kappa}(T)$ as anticipated. $T_1(\delta)$ [see Fig. 7(d)] is then obtained by fitting each Fourier component by an exponential decay. T_1 increases with δ as expected from Eq. 14, although it does not exactly follow the Purcell effect.

To understand this discrepancy, we perform numerical simulations, using the estimated $\rho_g(g)$ and a constant ρ_δ as already discussed, and without any adjustable parameter. We first compute the time traces $X_e(t + \tau)$, which

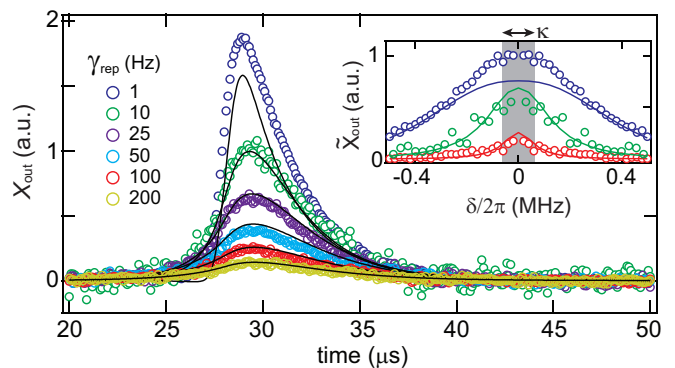


FIG. 8. Influence of Hahn echo sequence repetition rate γ_{rep} on measured (open symbols) and simulated (lines) echo shape $X_{\text{out}}(t)$ (device 2). Bump-shaped control pulses are used to generate $1\mu\text{s}$ -long intra-resonator pulses. Inset: Fourier transform of some of the echos in the main graph (corresponding symbols, lines and colors). The resonator linewidth is indicated by a dashed area.

we find in quantitative agreement with the data as seen in Fig. 7(a). We then Fourier transform the simulation result and extract $T_1(\delta)$ as for the experimental data. The result [see Fig. 7(b,d)] reproduces well the dependence of δ found in the experimental values. Detailed analysis of the simulation data shows that the finite width of the $\rho_g(g)$ distribution is actually causing the discrepancy with the Purcell effect: the large- δ components of the spin-echo come from spins more strongly coupled than those contributing to the $\delta = 0$ component.

We finally test the influence of the Hahn echo sequence repetition rate γ_{rep} on the temporal echo shape with device 2 (see Fig. 8). In order to maximize the spin excitation bandwidth, bump-shaped excitation pulses^{14,15} are used: they are designed to make the intra-resonator field closely approximates a rectangular shape with rise and fall times much shorter than the cavity damping time $2/\kappa$, which thus brings the experiment closer to the idealized quasi-instantaneous pulse limit discussed in section II. More quantitatively, the intra-resonator field pulse length is $1\mu\text{s}$, resulting in an excitation bandwidth of $\approx 1\text{MHz}$ (whereas $\kappa/2\pi = 100\text{kHz}$). At constant induced spin flip angle, the maximum amplitude of a bump pulse is consequently much larger than for a square pulse.

Figure 8 shows that both the risetime and maximum height of the echo decrease with increasing γ_{rep} . In particular, the rise becomes faster than $2/\kappa$ at $\gamma_{\text{rep}} = 1\text{Hz}$, which confirms spin excitation outside the resonator bandwidth. The echo emission is however inevitably filtered by the cavity and the echo-shape follows a cavity ring-down with time constant $\sim 2/\kappa$. Once again, numerical simulations (see Fig. 8) capture the changes in echo-shape and magnitude. Similar to device 1, the pulse amplitude for device 2 ($\beta = 5 \times 10^6\text{ s}^{-1/2}$) is estimated from corresponding Rabi and T_1 measurements ($\approx 30\text{ms}$, extracted using square pulses).

V. CONCLUSION

We have explored theoretically and experimentally the consequences of spin relaxation by the Purcell effect on the temporal shape and amplitude of spin echoes in a number of experimental situations. Such effects arise from the correlations between relaxation time of a given spin packet, its detuning to the resonator, and its spin-photon coupling constant (or equivalently its Rabi frequency).

When the spin-resonator coupling is distributed inhomogeneously, as is commonly the case for microresonators, the sub-ensemble of spins which contribute most strongly to the measured signal is determined by the pulse amplitude (i.e. with more weakly coupled spins measured for stronger pulses, and vice versa). In the Purcell regime for spin relaxation, the measured spin relaxation time is a strong function of the spin-resonator coupling, and hence, of the pulse amplitudes used.

When the spin linewidth is broader than the resonator linewidth, the relaxation time of the spin-echo Fourier components varies quadratically with detuning, which leads to a repetition-time-dependent shape for the spin-echo. When on the other hand both the coupling and detuning are well-defined, which can be achieved with careful design of the microresonator and sample geometries, typical pulse EPR results are recovered, although with a relaxation time determined by the Purcell effect.

Microresonators are becoming of increasing importance in EPR as part of a push for greater spin number sensitivity. However, the combination of inhomogeneous spin-resonator coupling and the introduction of resonator-induced spin relaxation via the Purcell effect, lead to general and significant influences in the measured spin-echo shapes and decay profiles. Such effects require careful treatment and understanding when analysing EPR data in this regime, and motivate, where possible, design of sample and resonator geometries to minimise their influence on conventional EPR measurements. More generally, these qualitatively novel effects confirm that Purcell relaxation constitutes a novel regime for magnetic resonance that deserves deeper exploration on its own.

ACKNOWLEDGEMENT

We thank P. Sénat, D. Duet and J.-C. Tack for the technical support, and are grateful for fruitful discussions within the Quantronics group. We acknowledge IARPA and Lincoln Labs for providing a Josephson Traveling-Wave Parametric Amplifier used in some of the measurements. We acknowledge support of the European Research Council under the European Community's Seventh Framework Programme (FP7/2007-2013) through grant agreement No. 615767 (CIRQUSS), and of the Agence Nationale de la Recherche under the Chaire Industrielle NASNIQ. AD acknowledges a SNSF mobility

fellowship (177732).

REFERENCES

- ¹A. Schweiger and G. Jeschke, *Principles of pulse electron paramagnetic resonance* (Oxford University Press, 2001).
- ²A. M. Tyryshkin, S. Tojo, J. J. L. Morton, H. Riemann, N. V. Abrosimov, P. Becker, H.-J. Pohl, T. Schenkel, M. L. W. Thewalt, K. M. Itoh, and S. A. Lyon, *Nat Mater* **11**, 143 (2012).
- ³J. L. Du, G. R. Eaton, and S. S. Eaton, *Journal of Magnetic Resonance, Series A* **115**, 213 (1995).
- ⁴I. V. Koptug, S. H. Bossmann, and N. J. Turro, *Journal of the American Chemical Society* **118**, 1435 (1996).
- ⁵A. Doll, S. Pribitzer, R. Tschaggelar, and G. Jeschke, *Journal of Magnetic Resonance* **230**, 27 (2013).
- ⁶E. M. Purcell, *Phys. Rev.* **69**, 681 (1946).
- ⁷P. Goy, J. M. Raimond, M. Gross, and S. Haroche, *Physical Review Letters* **50**, 1903 (1983).
- ⁸S. Haroche and J. M. Raimond, *Exploring the quantum* (Oxford University Press, 2006).
- ⁹A. Bienfait, J. Pla, Y. Kubo, M. Stern, X. Zhou, C.-C. Lo, C. Weis, T. Schenkel, M. Thewalt, D. Vion, D. Esteve, B. Julsgaard, K. Moelmer, J. J. L. Morton, and P. Bertet, *Nature Nanotechnology* **11**, 253 (2015).
- ¹⁰S. Probst, A. Bienfait, P. Campagne-Ibarcq, J. J. Pla, B. Albanese, J. F. D. S. Barbosa, T. Schenkel, D. Vion, D. Esteve, K. Moelmer, J. J. L. Morton, R. Heeres, and P. Bertet, *Applied Physics Letters* **111**, 202604 (2017).
- ¹¹A. Bienfait, J. Pla, Y. Kubo, X. Zhou, M. Stern, C.-C. Lo, C. Weis, T. Schenkel, D. Vion, D. Esteve, J. Morton, and P. Bertet, *Nature* **531**, 74 (2016).
- ¹²C. Eichler, A. J. Sigillito, S. A. Lyon, and J. R. Petta, *Phys. Rev. Lett.* **118**, 037701 (2017).
- ¹³B. Albanese, S. Probst, V. Ranjan, C. Zollitsch, M. Pechal, A. Wallraff, J. Morton, D. Vion, D. Esteve, E. Flurin, and P. Bertet, *arXiv:1910.11092 [cond-mat, physics:quant-ph]* (2019), arXiv: 1910.11092.
- ¹⁴Q. Ansel, S. Probst, P. Bertet, S. J. Glaser, and D. Sugny, *Phys. Rev. A* **98**, 023425 (2018).
- ¹⁵S. Probst, V. Ranjan, Q. Ansel, R. Heeres, B. Albanese, E. Albertinale, D. Vion, D. Esteve, S. J. Glaser, D. Sugny, and P. Bertet, *Journal of Magnetic Resonance* **303**, 42 (2019).
- ¹⁶C. W. Gardiner and M. J. Collett, *Physical Review A* **31**, 3761 (1985).
- ¹⁷N. Bloembergen and R. V. Pound, *Physical Review* **95**, 8 (1954).
- ¹⁸B. Julsgaard, C. Grezes, P. Bertet, and K. Moelmer, *Physical Review Letters* **110**, 250503 (2013).
- ¹⁹Y. Tabuchi, M. Negoro, K. Takeda, and M. Kitagawa, *Journal of Magnetic Resonance* **204**, 327 (2010).
- ²⁰A. L. Bloom, *Physical Review* **98**, 1105 (1955).
- ²¹J. Pla, A. Bienfait, G. Pica, J. Mansir, F. Mohiyaddin, Z. Zeng, Y. Niquet, A. Morello, T. Schenkel, J. Morton, and P. Bertet, *Physical Review Applied* **9**, 044014 (2018).
- ²²G. Feher, *Phys. Rev.* **114**, 1219 (1959).
- ²³J. Mansir, P. Conti, Z. Zeng, J. Pla, P. Bertet, M. Swift, C. Van de Walle, M. Thewalt, B. Sklenard, Y. Niquet, and J. Morton, *Physical Review Letters* **120**, 167701 (2018).
- ²⁴P. Haikka, Y. Kubo, A. Bienfait, P. Bertet, and K. Moelmer, *Phys. Rev. A* **95**, 022306 (2017).
- ²⁵X. Zhou, V. Schmitt, P. Bertet, D. Vion, W. Wustmann, V. Shumeiko, and D. Esteve, *Phys. Rev. B* **89**, 214517 (2014).
- ²⁶C. Macklin, K. O'Brien, D. Hover, M. E. Schwartz, V. Bolkhovskiy, X. Zhang, W. D. Oliver, and I. Siddiqi, *Science* **350**, 307 (2015).
- ²⁷M. H. Mohammady, G. W. Morley, and T. S. Monteiro, *Physical Review Letters* **105** (2010), 10.1103/physrevlett.105.067602.

Appendix A: Numerical simulations

For the numerical simulations presented in the main text, we have taken 600 discrete bins for Larmor frequency distribution δ_j linearly spaced between -5κ and 5κ . Furthermore, spin linewidths are much larger than κ and Rabi frequency, so we assume a constant spin distribution ρ_δ . The distribution in coupling strength is incorporated by taking 150 bins of g values, again linearly spaced between the maximum and the minimum value. The coupling strength distribution $\rho_g(g)$ is determined using a finite-element simulation of the magnetic field profile $\delta B_1(r)$ around the inductance (using COMSOL) and also the knowledge of the implantation profile below the inductor (measured by Secondary Ions Mass Spectroscopy). The minimum g is determined by the lateral size of the box in the COMSOL simulation, which we choose to be four times the width of the inductor while centered around the inductor. These boxes are shown in the Fig. 3(d-f). Since all measurements are done at low temperatures 20 mK and at large frequencies $\omega_0/2\pi \sim 7$ GHz, we take equilibrium polarization to be 1. However, because of finite repetition rate γ_{rep} , the initial conditions for the simulations are set by $S_z^{(j)}(t=0) = 1 - \exp[-1/(T_1^{(j)}\gamma_{\text{rep}})]$, $S_x^{(j)}(0) = S_y^{(j)}(0) = 0$.

Appendix B: Spin Hamiltonian of Bismuth donors in silicon

Implanted bismuth donors are substitutional impurities in the tetravalent silicon lattice. At low temperatures, the extra fifth electron stays bound to the Bi nucleus due to the Coulomb potential in a manner similar to the electron in the hydrogen atom²². The spin Hamiltonian H_{Bi} of an isolated bismuth donor subject to a magnetic field B_0 applied along the z axis is given by

$$H_{\text{Bi}} = \mathbf{A}\mathbf{S} \cdot \mathbf{I} + \omega_e(S_z - \delta I_z), \quad (\text{B1})$$

where \mathbf{S} is the spin-1/2 operator of the donor electron, \mathbf{I} is the nuclear spin operator of the Bismuth nucleus (with $I = 9/2$), $\omega_e = \gamma_e B_0$, $\delta = \gamma_n/\gamma_e$, and $\gamma_e/2\pi = 28$ GHz/T and $\gamma_n/2\pi = 6.962$ MHz/T are respectively the electron and nuclear spin gyromagnetic ratios. The hyperfine coupling constant between the electron and nuclear spins of the bismuth donor is $A/2\pi = 1.4754$ GHz. We point out that the Hamiltonian does not contain

a nuclear quadrupolar term despite $I = 9/2$, thanks to the symmetry of the electronic wave function in the ground state. The Hamiltonian can be diagonalized numerically, yielding 20 eigenstates $|F, m\rangle$, where F is the eigenvalue of the total angular momentum $\mathbf{F} = \mathbf{S} + \mathbf{I}$ and m its projection on the z -axis. At high magnetic fields $B_0 > 300$ mT, eigenstates are in the Zeeman basis and only nuclear-spin preserving ESR transitions are allowed, i.e. $|F = 4, m - 1\rangle \iff |F = 5, m\rangle$. At

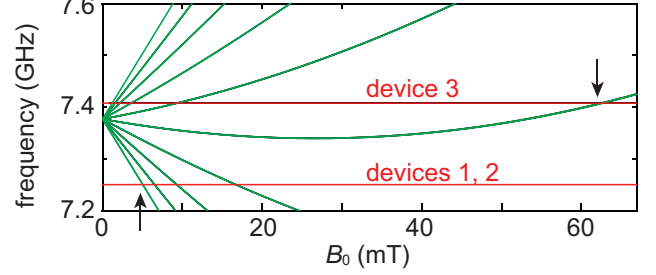


FIG. 9. Allowed S_x transition frequencies for Bi electron spins at low magnetic fields. Results shown in the main text are acquired for devices 1,2 near the first transition and for the device 3 near the fifth transition, as marked by arrows.

low fields, however, final eigenstates are strong hybridization of nuclear and electronic counterpart. Therefore all S_x transitions that satisfy $\Delta m = \pm 1$ are allowed and $|F = 4, m\rangle \iff |F = 5, m - 1\rangle$ transitions also become available. We note that for $|m| \leq 4$, two transitions described above are quasi-degenerate in energy. Different transitions however have different $\langle 0|S_x|1\rangle$ matrix elements. More details on energy levels in Bi can be found in the Ref. 27.

Accounting for degeneracies, ten ESR transitions are visible in Fig. 9. The resonance frequency of different devices is also shown. For devices 1 and 2, experiments are performed near the first transition $|F = 4, -4\rangle \iff |F = 5, -5\rangle$ that has a matrix element of 0.48. For device 3, data are obtained on degenerate transitions $|F = 4, -1\rangle \iff |F = 5, 0\rangle$ and $|F = 4, 0\rangle \iff |F = 5, -1\rangle$, each with a matrix element of 0.25. Different matrix elements for different transitions have been accordingly taken into account in the simulations. For all devices and all transitions, quantitative agreement is obtained between the measured relaxation times and the estimated Purcell times, without adjustable parameter, which brings further confirmation that the donors are indeed in the Purcell regime.